Seismic Gradiometry using Ambient Seismic Noise in an Anisotropic Earth

Citation for published version:
De Ridder, S & Curtis, A 2017, 'Seismic Gradiometry using Ambient Seismic Noise in an Anisotropic Earth', *Geophysical Journal International*, vol. 209, no. 2, pp. 1168-1179. https://doi.org/10.1093/gji/ggx073

Digital Object Identifier (DOI):
10.1093/gji/ggx073

Published In:
Geophysical Journal International

submitted to *Geophys. J. Int.*

Seismic Gradiometry using Ambient Seismic Noise in an Anisotropic Earth

S.A.L. de Ridder[1] and A. Curtis[2]

[1] *School of Mathematics and Maxwell Institute for Mathematical Sciences, University of Edinburgh, Edinburgh EH9 3FD, United Kingdom.*

[2] *School of GeoSciences and Grant Institute of Earth Science, University of Edinburgh, Edinburgh EH9 3FE, United Kingdom.*

Received 2017 February 17; in original form 2016 September 7

SUMMARY

We introduce a wavefield gradiometry technique to estimate both isotropic and anisotropic local medium characteristics from short recordings of seismic signals by inverting a wave equation. The method exploits the information in the spatial gradients of a seismic wavefield that are calculated using dense deployments of seismic arrays. The application of the method uses the surface wave energy in the ambient seismic field. To estimate isotropic and anisotropic medium properties we invert an elliptically anisotropic wave equation. The spatial derivatives of the recorded wavefield are evaluated by calculating finite differences over nearby recordings, which introduces a systematic anisotropic error. A two step approach corrects this error: finite difference stencils are first calibrated, then the output of the wave-equation inversion is corrected using the linearized impulse response to the inverted velocity anomaly. We test the procedure on ambient seismic noise recorded in a large and dense ocean bottom cable array installed over Ekofisk field. The estimated azimuthal anisotropy forms a circular geometry around the production-induced subsidence bowl. This conforms with results from studies employing controlled sources, and with interferometry correlating long records of seismic noise. Yet in this example, the results where obtained using only a few minutes of ambient seismic noise.

Key words: Surface waves and free oscillations; Seismic anisotropy; Seismic noise; Seismic tomography; Seismic interferometry; Wave propagation

1 INTRODUCTION

Knowledge of the subsurface stress state and material properties is key to understanding a range of earth-scientific phenomena such as earthquake and landslide nucleation, drilling and shallow-gas hazards, induced seismicity, and many other types of deformation and material failure. Variations of stress state are known to cause concomitant variations in elastic moduli, and these properties in turn affect the speed of elastic waves propagating through the medium (Brenguier et al., 2008; Korneev & Glubokovskikh, 2013; Brenguier et al., 2014; Hobiger et al., 2016). In particular, the orientation and magnitude of stress and the alignment of crystal orientation, pores, or layering, causes the wave speed to vary with direction of propagation, a property known as anisotropy (Crampin et al., 1980a; Teanby et al., 2004; Boness & Zoback, 2004; Herwanger & Horne, 2009). Measurements of both isotropic and anisotropic seismic velocities therefore place constraints on these various phenomena.

One of the first observations of anisotropy were incompatibilities of Love and Rayleigh wave dispersion curves (Anderson, 1961), and manifestations of shear wave splitting (Ando, 1980; Crampin et al., 1980b; Vennik et al., 1989). These observations were treated as point measurements indicating the properties underneath the stations. With increasing station coverage shear wave splitting maps now reveal anisotropy over large regions (Wüstefeld et al., 2009). Anisotropy in the crust and upper mantle has been linked to mantle flow (Peselnick & Nicolas, 1978; Christensen & Lundquist, 1982; Tanimoto & Anderson 1984). Maps of Rayleigh and Love wave anisotropic phase velocity in the upper mantle are found by tomography inverting large sets of observations covering different azimuths (Montagner & Jobert, 1988; Montagner & Nataf, 1988; Montagner & Tanimoto, 1990), potentially followed by a depth inversion to map anisotropy with depth (Montagner & Nataf 1986). More recently, finite frequency sensitivity kernels are proposed for full waveform inversion strategies to recover anisotropic elastic structure from surface waves (Sieminski et al., 2007; Plessix & Cao, 2011). In principle two linear orthogonal arrays can reveal the principal component of anisotropy, but with two dimensional arrays we can derive a more sophisticated azimuthal dependence of surface wave velocity (Forsyth & Li, 2013).

Observed gradients of propagating and standing seismic wavefields are known to contain important information about for example the wave propagation direction, and the medium properties. Wavefield gradiometry, literally, is the estimation or observation of a wavefield's spatial-gradients. When dense measurements are available throughout a larger region, the observations of temporal and spatial gradients can be exploited as local constraints in an inverse problem to estimate medium properties throughout the region. This is in contrast to other classes of geophysical inversion techniques such as tomography and full-waveform inversion, where the observations are posed as global constraints in an inverse problem for the medium parameters.

Curtis & Robertsson (2002) proposed to directly extract isotropic P- and S-velocities from observed three-dimensional derivatives of a wavefield. However the volumetric (tetrahedral) recordings required in order to estimate all such gradients, are rarely available as dense deployments of receivers are usually confined to the Earth's surface. Muijs et al. (2003) showed that for plane waves, gradiometry could be accomplished on the seabed using planar sensor arrays. Langston (2007a; 2007b; 2007c) and Poppeliers et al. (2013) extracted ray parameters and wave directionality from non-overlapping plane waves. However, the assumption of observing non-interfering plane-waves limits the use of wavefield gradiometry to simple wavefields where specific arrivals can be identified and isolated. A direct estimate for the phase velocity can also be recovered by inverting an eikonal equation for the travel-times of large earthquake surface wave arrivals, or of virtual seismic sources obtained by noise-correlations (Lin & Ritzwoller, 2011; Gouédard et al., 2012; De Ridder et al., 2015). These techniques are referred to as eikonal or Helmholtz tomography. They were applied on cross-correlations of ambient noise recorded by a large and dense ocean bottom cable (OBC) array installed over Valhall. OBC is a cable-based seismic receiver system laid down temporarily on the seafloor, or installed more permanently trenched a meter deep into the sea floor. De Ridder & Dellinger (2011) and Mordret et al. (2013a) found high resolution images of near-surface Scholte wave velocity, including anisotropy (Mordret et al., 2013b) at Valhall. Liu & Holt (2015) described a link between Helmholtz tomography and wavefield gradiometry, as applied to plane waves from large earthquakes. However, these approaches require identification of an arrival time limiting applications to large earthquakes, or requiring observations of long time series if estimated Greens functions derived from cross-correlation of ambient noise are to be used.

De Ridder & Biondi (2015b) introduced a gradiometry method applicable for surface-wave seismic noise by inverting a two dimensional scalar wave equation for isotropic wave velocities. They found that the error in the spatial finite difference approximation for the Laplacian operator can result in large velocity errors, especially when employing second order derivatives. Edme & Yuan (2016) extracted surface wave dispersion curves directly from seismic noise by following the plane wave gradiometry approach of Langston (2007b), analyzing the statistics of the first-order derivatives, to identify and discard time-windows with multiple interfering arrivals. Sollberger et al. (2016) employed seismic wavefield gradiometry to extract shear-wave information on the shallow lunar crust from the recordings of the Apollo active seismic experiment.

Whereas the wave equation inversion methodology by Curtis & Robertsson (2002) and De Ridder & Biondi (2015b) apply to ambient seismic noise, they were not designed for anisotropic media. Here, we propose a more general formulation that accounts for anisotropy in elastodynamic media. Then we introduce a practical formulation for surface waves in azimithal anisotropic media, and we propose a method that corrects the bias in the isotropic analysis revealing the anisotropy of the medium. We show how the anisotropic velocity errors caused by finite difference approximations of spatial derivatives can be corrected using a two step workflow. To illustrate the efficacy of this technique we carried out a field data study using ambient seismic noise recordings made in a large and dense OBC array installed over

Ekofisk field in the Norwegian North Sea (Eriksrud, 2010). These results are consistent with those obtained from active source data, even though we used data containing only 10 minutes of ambient noise recordings.

2 SEISMIC GRADIOMETRY

The term seismic gradiometry refers to the measurement or estimation of seismic wavefield gradients. These can be used for wavefield separation, estimation of propagation directions, or inversion for material properties. Here, we estimate the medium properties in the vicinity of each recording station directly from spatial and temporal gradients of the seismic recordings according to the wave equation. This was first referred to as *wave equation inversion* (Curtis & Robertsson, 2002) and later simply as *wavefield gradiometry* (Langston, 2007a). In this study we will refer to *(seismic wavefield) gradiometry* to avoid confusion between wave equation inversion and full waveform inversion.

A general formulation for elastodynamic wavefields could be based on the wave equation for the particle velocity:

$$\rho^{-1} C_{ijkl} \partial_j \partial_l u_k(\mathbf{x}, t) = \partial_t \partial_t u_i(\mathbf{x}, t) \tag{1}$$

where $\rho = \rho(\mathbf{x})$ is the bulk density and $C_{ijkl} = C_{ijkl}(\mathbf{x})$ is the elastic stiffness, and u_i with (in this equation only) $i = 1, 2, 3$ are the three components of particle velocity and (in this equation only) we used the Einstein summation convention. It is possible to invert this equation for local medium parameters directly when measurements of all three components of the state vector are available at neighbouring points throughout a volume, since then the derivatives in eq. (1) can be estimated using finite difference in space and time. We recognize the problem then takes the form

$$\mathbf{F}_i \ \mathbf{m} = \mathbf{b}_i \tag{2}$$

in which the subscript indicates a particular time-slice and $\mathbf{m}$ describes the material density and stiffness ratios $\rho^{-1} C_{ijkl}$. In principle, when sufficient linearly independent wavestates are observed, this equation can be solved for all independent elements of the elasticity, scaled by the inverse of the density. However, inversion of eq. (1) for the medium parameters everywhere in a volume, requires recordings throughout the volume. Since recordings are usually confined to a surface, we focus on wave equation inversion for surface wave ambient noise. A technique to recover the isotropic phase velocity of surface waves directly from measured temporal and spatial gradients of an ambient noise wavefield was first formulated by De Ridder & Biondi (2015b). We briefly review the theory for isotropic gradiometry then formulate elliptically anisotropic wavefield gradiometry.

2.1 Isotropic Gradiometry

When the ambient seismic field is dominated by Rayleigh or Scholte surface waves, the wavefield recorded in the vertical component of particle velocity or the pressure, may be approximated as a superposition of non-dispersive single-mode surface-wave plane waves in the far field. In practice this is achieved by filtering the data for a narrow frequency bandwidth to avoid dispersion effects, and neglecting the remaining energy associated with higher modes. Any superposition of such surface wave plane waves, including standing waves, satisfies the following two-dimensional scalar-wave equation:

$$M_0(x, y)\,[\partial_x\partial_x + \partial_y\partial_y]\,U(x, y, t) = \partial_t\partial_t U(x, y, t) \tag{3}$$

where $M_0(x, y)$ is the isotropic surface-wave phase velocity squared, $M_0(x, y) = c_0^2(x, y)$. This wave equation, and its associated eikonal equation, implicitly form the basis for many conventional imaging techniques for surface waves. The concepts of phase and group velocity tomography are based on two dimensional wave propagation through a map of effective phase and group velocities (Aki, 1957); Wielandt, 1993), the latest non-linear surface wave tomography approaches still rest on this principle (Galetti et al., 2015a), and array imaging techniques such as eikonal and Helmholtz tomography (Lin, Ritzwoller & Snieder, 2009; Lin & Ritzwoller, 2011; De Ridder et al., 2015) are based on an eikonal equation derived for a two-dimensional scalar-wave equation.

The state variable scalar field $U(x, y, t)$ is generally observed discretely in time and space, with regular sampling in time but irregular sampling in space. Dense observations provide an opportunity to estimate the second-order spatial derivatives of the wavefield by taking irregular finite differences between different nearby receivers and the time derivatives at each single station by standard finite differences. Consequently, the only unknown in eq. (3) is the wave speed.

We estimate the wave speed by inverting eq. (3) with additional regularization constraints. We pose the medium parameter as a perturbation on an average constant background value, $M_0(x,y) = \overline{M}_0 + \Delta M_0(x,y)$, and insert this into eq. (3) giving

$$\Delta M_0(x,y)\mathbf{D}_{\boldsymbol{\Delta}}\mathbf{U}_i = \ddot{\mathbf{U}}_i - \overline{M}_0\mathbf{D}_{\boldsymbol{\Delta}}\mathbf{U}_i \tag{4}$$

where $\mathbf{U}_i$ is a vector containing the observations at all stations for the i^{th} time sample (from hereon the subscript i denotes time sample), and $\mathbf{D}_{\boldsymbol{\Delta}}$ denotes a discrete Laplace operator which calculates spatial derivatives for all elements of $\mathbf{U}_i$, we constructed this operator following Huiskamp (1991). This wave equation has the form $\mathbf{F}_i\,\mathbf{m} = \mathbf{b}_i$, where the subscript denotes a specific observed state of the wavefield at a different time, and with

$$\mathbf{F}_i = \mathrm{diag}\left\{\mathbf{D}_{\boldsymbol{\Delta}}\mathbf{U}_i\right\} \tag{5}$$

$$\mathbf{b}_i = \ddot{\mathbf{U}}_i - \overline{M}_0\mathbf{D}_{\boldsymbol{\Delta}}\mathbf{U}_i \tag{6}$$

$$\mathbf{m} = \Delta\mathbf{M}_0 \tag{7}$$

where diag{ } denotes a diagonal matrix formed with the input vector on the diagonal, and $\ddot{\mathbf{U}}$ denotes the second order derivative in time. The size of the matrices indicates the size of the model space: $\mathbf{F}$ in eq. (5) has dimensions $M \times M$, where M is the number of model parameters in $\mathbf{m}$ (equating to the total number of stations at locations (x,y) in eq. 4). We zero the rows in $\mathbf{F}_i$ and $\mathbf{b}_i$ concerning station locations for which we could not obtain a reliable finite difference stencil. The presence of diagonal matrices in the linear system indicates that in the absence of regularization, all model parameters are constrained independent. However, given N observations of states of the wavefield we invert the system by least-squares regression, adding additional constraints by 0^{th} and 2^{nd}-order Tikhonov regularization

$$\left[\sum_{i=1}^{N}\mathbf{F}_i^T\mathbf{F}_i+\epsilon_1\mathbf{D_\Delta}^T\mathbf{D_\Delta}+\epsilon_2\mathbf{I}\right]\mathbf{m}=\sum_{i=1}^{N}\mathbf{F}_i\mathbf{b}_i \tag{8}$$

where $\mathbf{I}$ is an identity matrix, and ϵ_1 and ϵ_2 are the regularization strengths. When $\epsilon_1=\epsilon_2=0$ eq. (8) reduces to a simple regression at each station of the array. In the examples in this study, we selected ϵ_1 by comparing the reduction of the variance of the model space versus increasing regularization strength with an L-curve criteria (Hansen & OLeary, 1993; Lawson & Hanson, 1974). We found the result not to vary on the particular value of ϵ_2 and set ϵ_2 to 10^{-15}. We solve equation 8 by LU decomposition of the composite matrix on the left-hand side of eq. (8). Using finite differences to estimate the spatial derivative assumes the medium parameters do not vary over the spatial stencil spread. In practice the smoothness of the recovered velocity map will be a function of regularization strength, and the spatial stencil spread forms an upper bound on the resolution.

2.2 Anisotropic Gradiometry

We now extend the formulation to include azimuthal anisotropy. We describe the anisotropy in local propagation velocity, $c=c(x,y,\phi)$, of planar surface-waves as elliptical as a function of azimuth:

$$c^2(\phi)=c_f^2\,\sin^2(\phi-\alpha)+c_s^2\,\cos^2(\phi-\alpha) \tag{9}$$

where c_f and c_s are the fast and slow magnitudes of the anisotropic velocity, and α is the direction of fast. This form closely resembles the slightly anisotropic Rayleigh phase velocity azimuthal anisotropy discussed by Smith & Dahlen (1973) when we omit the 4ϕ term, see Appendix A in De Ridder et al. (2015), when data quality does not permit this0term to be fit (Lin et al., 2009; Mordret et al., 2013b). Elliptical anisotropy describes SH-wave anisotropy in tilted transversely isotropic media (Tsvankin, 2011), and the elegant properties of ellipses has been a popular choice for approximately representing anisotropy in other wavefields and media (Helbig, 1983; Dellinger, 1991). Dropping the 4ϕ term or for Rayleigh and Scholte wave anisotropy when.

We aim to derive a scalar wave-equation suitable for seismic noise, filtered to pass a narrow frequency range so that we can ignore the frequency dependence in the derivation. To derive an elliptically anisotropic form of eq. (3), we substitute $c^2(\phi)$ into a general dispersion relationship $c^2(\phi)\,|\mathbf{k}|^2 = \omega^2$, where $\mathbf{k} = [k_x, k_y]^T$ is the wavenumber vector. Using the trigonometric relationships $\cos(\phi-\alpha) = \cos(\phi)\cos(\alpha) + \sin(\phi)\sin(\alpha)$, $\sin(\phi-\alpha) = \sin(\phi)\cos(\alpha) - \cos(\phi)\sin(\alpha)$ and $\cos^2(\alpha) + \sin^2(\alpha) = 1$, we find:

$$\omega^2 = M_{11}k_xk_x + (M_{12} + M_{21})\,k_xk_y + M_{22}k_yk_y \tag{10}$$

where $k_x = |\mathbf{k}|\sin(\phi)$ and $k_y = |\mathbf{k}|\cos(\phi)$. The elements M_{11}, $M_{12} = M_{21}$, and M_{22} form the elements of a two-by-two matrix $\mathbf{M}$, and are a function of c_f, c_s, and α:

$$M_{11} = (c_f^2 - c_s^2)\,\sin^2(\alpha) + c_s^2 \tag{11}$$

$$M_{12} = (c_f^2 - c_s^2)\,\sin(\alpha)\cos(\alpha) \tag{12}$$

$$M_{22} = (c_f^2 - c_s^2)\,\cos^2(\alpha) + c_s^2 \tag{13}$$

The eigenvalues of the matrix $\mathbf{M}$ are c_f^2 and c_s^2, and the eigenvectors indicate the fast and slow directions. In this manuscript we graphically display the anisotropic medium parameters as an isotropic component defined by ${}^1\!/_2\,(c_f + c_s)$ and a magnitude anisotropy in percent defined by $50 \times (c_f - c_s)\,(c_f + c_s)^{-1}$. Performing a spatial and temporal inverse Fourier transformation, we find the wave-equation operator that acts on the state variable $U(x, y, t)$ in an elliptically anisotropic scalar wave equation:

$$[M_{11}(x,y)\ \partial_x\partial_x + (M_{12}(x,y) + M_{21}(x,y))\ \partial_x\partial_y + M_{22}(x,y)\ \partial_y\partial_y]\ U(x,y,t) = \partial_t\partial_t U(x,y,t) \tag{14}$$

which alternatively can be written in the following matrix form:

$$\begin{bmatrix} \partial_x & \partial_y \end{bmatrix} \begin{bmatrix} M_{11}(x',y') & M_{12}(x',y') \\ M_{21}(x',y') & M_{22}(x',y') \end{bmatrix} \begin{bmatrix} \partial_x \\ \partial_y \end{bmatrix} U(x,y,t) = \partial_t\partial_t U(x,y,t) \tag{15}$$

where the presence of a prime on the spatial coordinates of the medium parameters denotes that the spatial derivative operators do not operate on the medium parameters, but only on the wavefield. In a strict sense we neglected lateral velocity variations in the derivation of eq. (14), and thus neglected lateral surface wave scattering. However by allowing the medium parameters to vary as a function of space, we do allow a degree of scattering just as the isotropic two-dimensional wave eq. (3) still allows scattering due to lateral velocity variations.

Similarly to the isotropic case, we use the nearby stations to evaluate spatial finite differences. In the absence of noise, we would need three linearly independent realizations of wave states to resolve all three unknowns in eq. (14). Similarly to the isotropic case we pose the medium parameter as a perturbation on the isotropic value, $\mathbf{M}(x,y) = \mathbf{I}M_0(x,y) + \Delta\mathbf{M}(x,y)$, where $\mathbf{I}$ is a two-by-two identity matrix:

$$\Delta M_{11}(x,y)\mathbf{D_{xx}}\mathbf{U}_i + \left[\Delta M_{12}(x,y) + \Delta M_{21}(\mathbf{x})\right]\mathbf{D_{xy}}\mathbf{U}_i + \Delta M_{22}(x,y)\mathbf{D_{yy}}\mathbf{U}_i = \ddot{\mathbf{U}}_i - M_0(x,y)\mathbf{D_{\Delta}}\mathbf{U}_i \tag{16}$$

Here $\mathbf{D_{xx}}$, $\mathbf{D_{yy}}$, and $\mathbf{D_{xy}}$ denote discrete second-order spatial derivative operators with subscripts indicating the spatial directions, and $\mathbf{D_{\Delta}}$ is as before and also equates to $\mathbf{D_{\Delta}} = \mathbf{D_{xx}} + \mathbf{D_{yy}}$. This equation, similar to the isotropic case, has the form $\mathbf{F}_i\ \mathbf{m} = \mathbf{b}_i$, but the elements of this linear system are:

$$\mathbf{F}_i = \left[\ \mathrm{diag}\left\{\mathbf{D_{xx}}\mathbf{U}_i\right\},\quad 2\ \mathrm{diag}\left\{\mathbf{D_{xy}}\mathbf{U}_i\right\},\quad \mathrm{diag}\left\{\mathbf{D_{yy}}\mathbf{U}_i\right\}\ \right] \tag{17}$$

$$\mathbf{b}_i = \ddot{\mathbf{U}}_i - \mathrm{diag}\left\{\mathbf{M_0}\right\}\mathbf{D_{\Delta}}\mathbf{U}_i \tag{18}$$

$$\mathbf{m} = \left[\ \boldsymbol{\Delta}\mathbf{M_{11}},\quad \boldsymbol{\Delta}\mathbf{M_{12}},\quad \boldsymbol{\Delta}\mathbf{M_{22}}\ \right]^T \tag{19}$$

Here, the number of model parameters is three times that in the linear system for the isotropic case, and $\mathbf{F}$ in eq. (17) has dimensions $M \times 3M$, where M is the number of stations in the array. If we make N observations of states of the wavefield, we can invert the system by least-squares regression, adding additional constraints by 0^{th} and 2^{nd}-order Tikhonov regularization:

$$\left[\ \sum_{i=1}^{N} \mathbf{F}_i^T\mathbf{F}_i + \epsilon_1\mathbf{D}^T\mathbf{D} + \epsilon_2\mathbf{I}\ \right]\mathbf{m} = \sum_{i=1}^{N}\mathbf{F}^T\mathbf{b}_i \tag{20}$$

where

$$\mathbf{D} = \begin{bmatrix} \mathbf{D}_{\boldsymbol{\Delta}} & 0 & 0 \\ 0 & \mathbf{D}_{\boldsymbol{\Delta}} & 0 \\ 0 & 0 & \mathbf{D}_{\boldsymbol{\Delta}} \end{bmatrix} \tag{21}$$

2.3 Inverting synthetic isotropic plane wave data

We use finite differences to evaluate the spatial derivatives, and consequently we introduce an error in the approximation of the continuous operators. These errors depend on the station geometry of the array, and on the effective spatial wavelength of the data. In this study we use a field dataset from Ekofisk's ocean bottom cable (OBC) array to evaluate the merit of our method. The station array has dense in-line and sparse cross-line station spacing, respectively 50 m and 300 m (Fig. 1). For further details on the array and field, see the field data example below. We computed stencils by inverting a second-order Taylor series expansion on the geometric distribution of the nearby stations (Huiskamp, 1991). For each station we select neighboring stations within a 400 m radius to form the stencil (e.g. black circle in Fig. 1), hence we cannot resolve anomalies smaller than ˜800 m in size. We discarded each station with fewer than 36 such neighboring stations to ensure a minimum quality of FD stencil. Thus we could not obtain reliable estimates near the edges of the array or in areas where the array was disrupted due to infrastructure. The blue stations in Fig. 1 indicate the station locations where we have a reliable finite difference stencil.

From a dispersion analysis by De Ridder & Biondi (2015b) we know that the surface waves observed in ambient noise at Ekofisk travel with an average velocity of approximately 490 m/s at 0.7 Hz, and are not aliased in the in-line or the cross-line direction. For each stencil in the array, we synthesize 36 sets of plane waves from different angles spaced 10 degrees apart, covering all 360 degrees, oscillating at 0.7 Hz with an isotropic moveout of 490 m/s.

This synthetic data is input into the two step algorithm for anisotropic gradiometry. We solved the linear inverse system (eq. 2) for isotropic velocities, with eqs. (5) to (7).

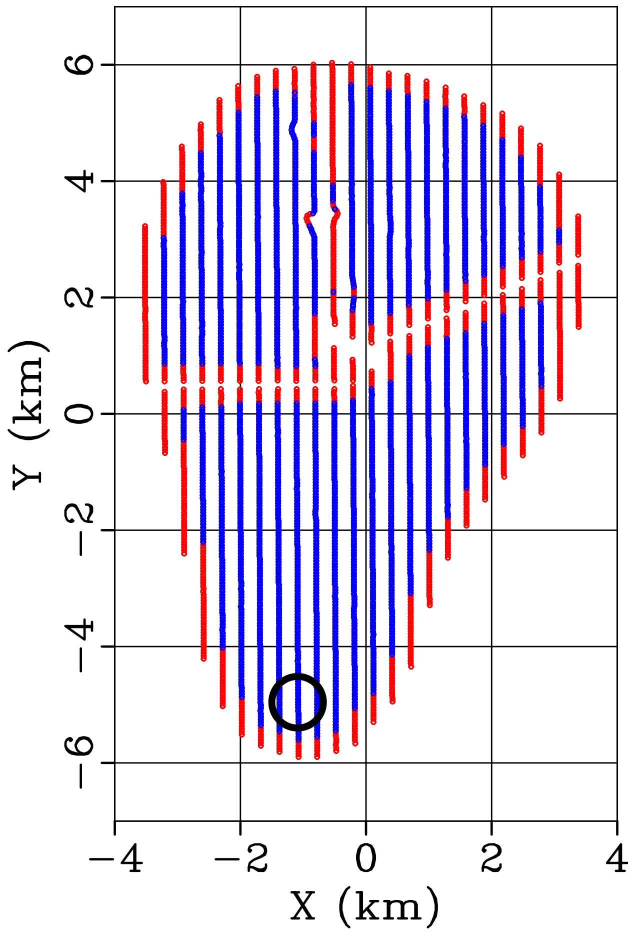

Figure 1. Station geometry of the ocean bottom cable (OBC) array installed at Ekofisk; stations are indicated by small red and blue circles. Blue circles indicate those stations where we have a reliable finite difference stencil using the nearby stations in a radius of 400 m (indicated for example by the black circle).

To resolve the spatially varying nature of the erroneous recovered anisotropic velocity, we used $\epsilon_1 = 0$. Secondly, we solved the linear system (eq. 2), with eqs. (17) to (19), for an anisotropic velocity map, using the solution of the isotropic case as the background velocity map (Fig. 2a). The colours indicate the isotropic component of the retrieved anisotropic velocities while the black dashes indicate the magnitude and fast-directions of anisotropy. Even though the inversion ought to result in a homogeneous isotropic velocity, the inversion yields (apparent) higher isotropic velocity and also include anisotropic components: this is the result of stencil error.

The stencil error is a function of the stencil spacing relative to the wavelength of the function being sampled. To visualize the error in second order finite difference stencils, we

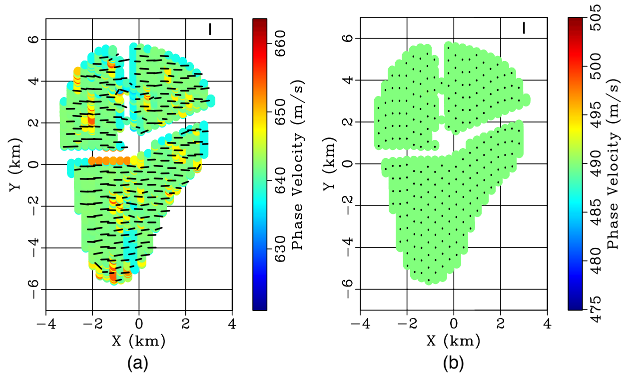

Figure 2. Synthetic data example using the station geometry of the Ekofisk OBC array, inverting data that represents recordings of monochromatic plane waves at 0.7 Hz propagating through a homogeneous and isotropic velocity structure of 490 m/s. Colour indicates isotropic component of velocity; dashes indicate magnitude and fast-direction of anisotropy (dash in upper right corner indicates 10% magnitude, the difference between maximum and minimum velocities as a percentage of the isotropic velocity). a) Apparent anisotropy observed using finite differences with second order accuracy (without correction). b) Observed homogeneous isotropic velocity map retrieved using finite differences with second order accuracy including a correction derived from the anisotropy observed in (a).

plot the Fourier-space spectrum of the stencil coefficients (computed by discrete Fourier transformation) with the ideal spectrum of the continuous operator ($|k|^2$) in Fig. 3. Notice that the error is zero for constant-functions, and is largest for wavelengths near Nyquist. The frequency of the data and the velocity of the medium determine the spatial wavelength of the wavefield along the horizontal axis of Fig. 3. The measurement of second order derivatives is plotted along the vertical axis of Fig. 3. Notice that we always underestimate the magnitudes of the second order derivatives. Thus we over-estimate the velocity by wavefield gradiometry, which essentially depends on the ratio between the second order time derivatives and the second order space derivatives. In two dimensions the stencil error is generally angle dependent. The stencil spacing is larger in the cross-line direction than the in-line direction, hence we find an erroneous apparent anisotropy with fast direction in the cross-line direction. Subsampling the in-line stations to approximately equalize the inline and cross-line station spacing resulted in using a much lower number of stations (samples)

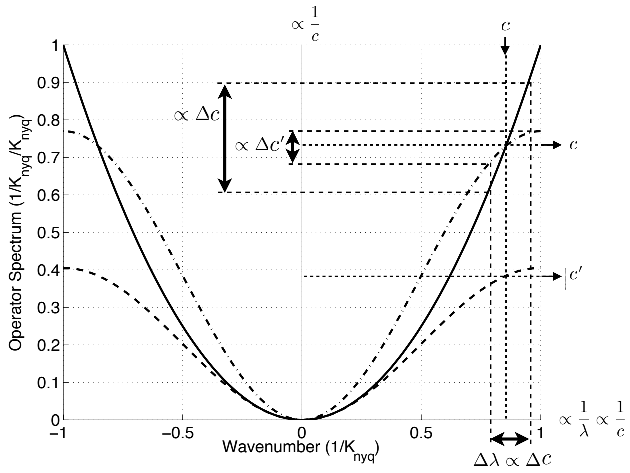

Figure 3. Spectra of the finite difference stencil for a second order derivative operator with second order accuracy. Solid line: spectrum of ideal continuous operator ($|-k^2| = k^2$). Dashed line: spectrum of the original finite difference stencil. Dash-dot line: spectrum of calibrated (by scaling) finite difference stencil. The effective wavelength of the wavefield determines the position on the horizontal axis, while the measured second order spatial derivative is plotted along the vertical axis. The error of the uncorrected finite difference stencil leads to an over estimation of the velocity $c' > c$. The scaled finite difference stencils lead to underestimation of the correct spread of the second order spatial derivatives due to a true velocity change, $\Delta c' < \Delta c$.

being used to measure the spatial gradients of the wavefield. This had an averse effect on the quality of the measurement of spatial derivatives and the resulting velocity field.

3 CORRECTION PROCEDURES FOR FINITE DIFFERENCES

Ellipses are attractive geometrical shapes to use for describing anisotropy because an ellipse can be turned into a circle or any other ellipse by an invertible linear transformation. We aim to establish a correction procedure for the finite difference stencils by approximating the angle dependent error as ellipsoidal, and inserting two Jacobians into eq. (15). In Fig. 2a we observed an apparent anisotropy, here denoted $\mathbf{M}_h(\mathbf{x})$, while we should have observed a homogeneous isotropic medium with parameters $\mathbf{C}_h(\mathbf{x}) = c_h^2\mathbf{I}$, with $c_h = 490$ m/s, everywhere and $\mathbf{I}$ a two-by-two identity matrix. The matrix $\mathbf{M}$ containing the elliptically anisotropic medium parameters is symmetric ($m_{12} = m_{21}$). For this matrix we write the eigenvalue-eigenvector decomposition as

$$\mathbf{M} = \mathbf{P}\mathbf{\Lambda}\mathbf{P}^T \tag{22}$$

where

$$\mathbf{P} = \begin{bmatrix} \mathbf{p}_1 & \mathbf{p}_2 \end{bmatrix} = \begin{bmatrix} p_{11} & p_{12} \\ p_{21} & p_{22} \end{bmatrix} \tag{23}$$

contains the unit-eigenvectors as columns and

$$\mathbf{\Lambda} = \begin{bmatrix} \lambda_1 & 0 \\ 0 & \lambda_2 \end{bmatrix} \tag{24}$$

contains the corresponding eigenvalues. To derive a calibration method from $\mathbf{M}_h$ we seek to define a particular combination, $\mathbf{J}$, of the scaled eigenvectors such that

$$\mathbf{J}^T\mathbf{C}_h\mathbf{J} = \mathbf{M}_h \tag{25}$$

If we define

$$\mathbf{S} = \begin{bmatrix} \sqrt{\lambda_1}/c_h & 0 \\ 0 & \sqrt{\lambda_2}/c_h \end{bmatrix} \tag{26}$$

then

$$\mathbf{M}_h = \mathbf{P}\mathbf{S}^T\mathbf{P}^T\mathbf{C}_h\mathbf{P}\mathbf{S}\mathbf{P}^T = \mathbf{J}^T\mathbf{C}_h\mathbf{J} \tag{27}$$

where $\mathbf{J}(\mathbf{x}) = \mathbf{P}(\mathbf{x})\mathbf{S}\mathbf{P}^T(\mathbf{x})$ with the property $\mathbf{J} = \mathbf{J}^T$.

Inserting eq. (25) into eq. (15) we see that $\mathbf{J}$ describes a rotation and a translation, and hence acts as a Jacobian (a standard, orthogonality-preserving transformation) on the coordinate system of the spatial derivative operators. This Jacobian contains scaled eigenvectors of the matrix $\mathbf{M}_h$. The scaling coefficient is the ratio between the square root of the relevant eigenvalue of $\mathbf{M}_h$, and the phase velocity used to compute the synthetic data from which we measured $\mathbf{M}_h$. Inclusion of both $\mathbf{P}$ and $\mathbf{P}^T$ in eq. (27) ensures that the orientation of the coordinate system of the anisotropic medium properties remains unaltered.

We could use this relation and correct the observed apparent anisotropy as a final step after the inversion for medium parameters. However, it is more prudent to use the Jacobian in the wave equation so that we can apply the regularization free from the effect of stencil errors. To derive a correction for the finite difference approximation of the Laplace operator, we evaluate:

$$\begin{bmatrix} \partial_x & \partial_y \end{bmatrix} \begin{bmatrix} J_{11} & J_{21} \\ J_{12} & J_{22} \end{bmatrix} \begin{bmatrix} J_{11} & J_{12} \\ J_{21} & J_{22} \end{bmatrix} \begin{bmatrix} \partial_x \\ \partial_y \end{bmatrix} \tag{28}$$

and find in discrete operator form:

$$\begin{aligned} &\left[\left(\mathrm{diag}\{\mathbf{J_{11}}\}^2 + \mathrm{diag}\{\mathbf{J_{12}}\}^2\right)\mathbf{D_{xx}} + \right. \\ &\quad \left(\mathrm{diag}\{\mathbf{J_{12}}\} + \mathrm{diag}\{\mathbf{J_{21}}\}\right)\left(\mathrm{diag}\{\mathbf{J_{11}}\} + \mathrm{diag}\{\mathbf{J_{22}}\}\right)\mathbf{D_{xy}} + \\ &\qquad \left.\left(\mathrm{diag}\{\mathbf{J_{22}}\}^2 + \mathrm{diag}\{\mathbf{J_{21}}\}^2\right)\mathbf{D_{yy}}\right] = \mathbf{D'_{\Delta}} \end{aligned} \tag{29}$$

The elements of the new linear system for isotropic gradiometry, in place of eqs. (5) and (6), simply have $\mathbf{D'_{\Delta}}$ instead of $\mathbf{D_{\Delta}}$. To find the modified linear system for anisotropic gradiometry, we insert $\mathbf{J}^T\mathbf{MJ}$ into eq. 15 and expand the matrix product to identify the elements:

$$\mathbf{F}_i = \begin{bmatrix} \mathrm{diag}\{\mathbf{F}_{1,i}\}, & 2\,\mathrm{diag}\{\mathbf{F}_{2,i}\}, & \mathrm{diag}\{\mathbf{F}_{3,i}\} \end{bmatrix} \tag{30}$$

with

$$\begin{aligned} \mathbf{F}_{1,i} = [&\mathrm{diag}\{\mathbf{J_{11}}\}\mathrm{diag}\{\mathbf{J_{11}}\}\mathbf{D_{xx}} + \mathrm{diag}\{\mathbf{J_{11}}\}\mathrm{diag}\{\mathbf{J_{12}}\}\mathbf{D_{xy}} + \\ &\mathrm{diag}\{\mathbf{J_{11}}\}\mathrm{diag}\{\mathbf{J_{21}}\}\mathbf{D_{xy}} + \mathrm{diag}\{\mathbf{J_{12}}\}\mathrm{diag}\{\mathbf{J_{12}}\}\mathbf{D_{yy}}]\,\mathbf{U}_i \end{aligned} \tag{31}$$

$$\begin{aligned} \mathbf{F}_{2,i} = [&\mathrm{diag}\{\mathbf{J_{21}}\}\mathrm{diag}\{\mathbf{J_{11}}\}\mathbf{D_{xx}} + \mathrm{diag}\{\mathbf{J_{11}}\}\mathrm{diag}\{\mathbf{J_{22}}\}\mathbf{D_{xy}} + \\ &\mathrm{diag}\{\mathbf{J_{21}}\}\mathrm{diag}\{\mathbf{J_{12}}\}\mathbf{D_{xy}} + \mathrm{diag}\{\mathbf{J_{12}}\}\mathrm{diag}\{\mathbf{J_{22}}\}\mathbf{D_{yy}}]\,\mathbf{U}_i \end{aligned} \tag{32}$$

$$\begin{aligned} \mathbf{F}_{3,i} = [&\mathrm{diag}\{\mathbf{J_{21}}\}\mathrm{diag}\{\mathbf{J_{21}}\}\mathbf{D_{xx}} + \mathrm{diag}\{\mathbf{J_{21}}\}\mathrm{diag}\{\mathbf{J_{22}}\}\mathbf{D_{xy}} + \\ &\mathrm{diag}\{\mathbf{J_{12}}\}\mathrm{diag}\{\mathbf{J_{22}}\}\mathbf{D_{xy}} + \mathrm{diag}\{\mathbf{J_{22}}\}\mathrm{diag}\{\mathbf{J_{22}}\}\mathbf{D_{yy}}]\,\mathbf{U}_i \end{aligned} \tag{33}$$

and

$$\begin{aligned} \mathbf{b}_i = \ddot{\mathbf{U}} - \mathrm{diag}\{\mathbf{M_0}\}&\left[\left(\mathrm{diag}\{\mathbf{J_{11}}\}^2 + \mathrm{diag}\{\mathbf{J_{12}}\}^2\right)\mathbf{D_{xx}} + \right. \\ &\quad \left(\mathrm{diag}\{\mathbf{J_{12}}\} + \mathrm{diag}\{\mathbf{J_{21}}\}\right)\left(\mathrm{diag}\{\mathbf{J_{11}}\} + \mathrm{diag}\{\mathbf{J_{22}}\}\right)\mathbf{D_{xy}} + \\ &\qquad \left.\left(\mathrm{diag}\{\mathbf{J_{22}}\}^2 + \mathrm{diag}\{\mathbf{J_{21}}\}^2\right)\mathbf{D_{yy}}\right]\mathbf{U}_i \end{aligned} \tag{34}$$

$$\mathbf{m} = \begin{bmatrix} \mathbf{\Delta M_{11}}, & \mathbf{\Delta M_{12}}, & \mathbf{\Delta M_{22}} \end{bmatrix}^T \tag{35}$$

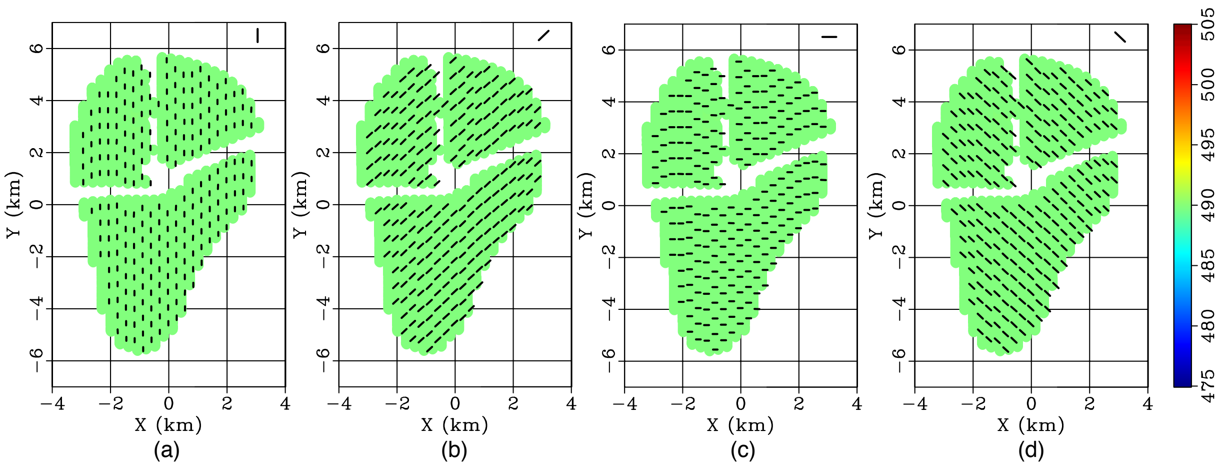

Figure 4. Synthetic data example using the station geometry of the Ekofisk OBC array, inverting monochromatic plane waves at 0.7 Hz with a homogeneous velocity of 490 m/s and 10% anisotropy in four directions: (a) 0°; (b) 45°; (c) 90°; (d) 135°. Colour indicates isotropic component of velocity; dashes indicate magnitude and fast-direction of anisotropy (dash in upper right corner indicates 10% magnitude).

We test these operators within the two step elliptically anisotropic gradiometry technique on the previous synthetic plane waves with an isotropic homogeneous moveout. We first solve the linear system (eq. 2) with eqs. (5) to (7) using eq. (29), and then solve the linear system (eq. 2) with eqs. (30) to (35), and recover almost exactly the correct velocity, up to a remnant average error of 0.007 % (Fig. 2b). To test whether we can recover anisotropy, we add 10% anisotropy (the difference between maximum and minimum velocities as a percentage of the isotropic velocity) in four different principal directions 0°, 45°, 90°, 135°. Fig. 4 shows that we can recover anisotropy in those principal directions throughout the maps: the remaining errors in the isotropic component and the angle are on average respectively 0.016% and 0.267°. However, we underestimate the magnitude of anisotropy by on average 47.45%.

We now test the ability to invert deviations from the velocity for which we calibrated the finite difference stencils (490 m/s). The velocity is varied according to a checkerboard pattern with a velocity anomaly of ±5% (Fig. 6a). The computations are kept simple by computing a set of plane waves for each subset of stations independently. Therefore, the test does not reveal any information regarding the lateral resolution of the recovered image, but does assess the ability to estimate velocities given the irregular stencil shapes around each location. The retrieved pattern shows that we significantly under estimate anomalies (Fig. 6b). The recovered positive anomalies have a 2.6% magnitude, while the recovered negative anomalies have a 2.4% magnitude. To understand this we analyse the spectra of the scaled finite difference stencils (Fig. 3). Although we corrected the error at a particular wavelength corresponding to a given velocity and frequency, for waves propagating with higher or lower velocities we will continue to respectively underestimate and overestimate the velocity. Fig. S1 in the supplementary material shows the error in retrieved isotropic anomaly and in anisotropic magnitude as a function of anomaly magnitude.

Finally, we test the effect of noise in wavefield gradiometry. Fig. 5 contains the results of a similar synthetic plane-wave data experiment as in Fig. 2, where we added Gaussian distributed noise to the synthetic plane wave data, with zero mean and a variance of 2% times the maximum amplitude. Despite that the added noise has zero mean, the inversion is biased towards higher velocities and includes an anisotropic component with the fast-direction aligning with the cross-line direction. We expect the bias to be a non linear function of the noise strength, and vary with the precise statistical characteristics of the noise. This bias diminishes our ability to iterate the calibration approach described above. Nevertheless, in the next section we propose a procedure to apply a correction to the recovered anisotropic velocity map.

3.1 Correction for specific anisotropic medium properties

The above procedure corrects the finite difference stencils, optimized for a specific isotropic velocity. We can generalize this procedure to correct the finite difference stencils for specific anisotropic medium properties. Say the true-target anisotropy is $\mathbf{M}_t$, but the estimated anisotropy without stencil correction is $\mathbf{M}_m$. The measured anisotropy can then be transformed into the true-target anisotropy by the following transform

$$\mathbf{M}_t = \mathbf{P}_t \mathbf{\Lambda}_t^{\frac{1}{2}} \mathbf{P}_t^T \mathbf{P}_m \mathbf{\Lambda}_m^{-\frac{1}{2}} \mathbf{P}_m^T \; \mathbf{M}_m \; \mathbf{P}_m \mathbf{\Lambda}_m^{-\frac{1}{2}} \mathbf{P}_m^T \mathbf{P}_t \mathbf{\Lambda}_t^{\frac{1}{2}} \mathbf{P}_t^T \tag{36}$$

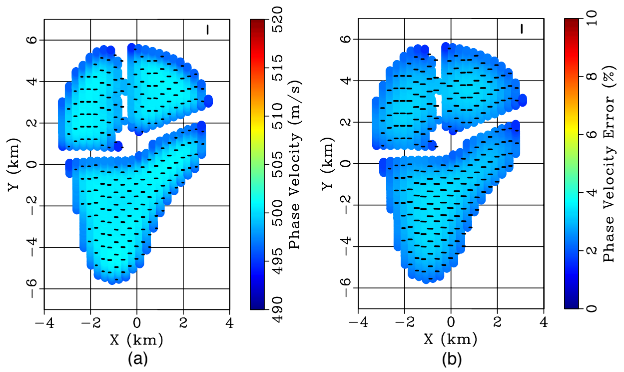

Figure 5. Synthetic data example displaying the effect of noise using the station geometry of the Ekofisk OBC array, inverting monochromatic plane waves at 0.7 Hz with a homogeneous and isotropic velocity of 490 m/s plus Gaussian distributed noise with a 2% variance. a) Recovered apparent anisotropic velocity map with linear scalebar in (m/s). b) Error in recovered apparent anisotropic velocities as a percentage of the true isotropic velocity. Dash in upper right corner indicates 10% anisotropy magnitude.

where the columns of $\mathbf{P}_t^T$ and $\mathbf{P}_m^T$ contain the eigenvectors of $\mathbf{M}_t$ and $\mathbf{M}_m$, while $\mathbf{\Lambda}_t$ and $\mathbf{\Lambda}_m$ are diagonal matrices with the eigenvalues of $\mathbf{M}_t$ and $\mathbf{M}_m$ on the diagonals. We recognize that $\mathbf{J}_m^{-1} = \mathbf{P}_m \mathbf{\Lambda}_m^{-\frac{1}{2}} \mathbf{P}_m^T$ is a Jacobian transforming the measured anisotropy into an isotropic unitary two-by-two matrix, and recognize that $\mathbf{J}_t = \mathbf{P}_t \mathbf{\Lambda}_t^{\frac{1}{2}} \mathbf{P}_t^T$ is a Jacobian that transforms the isotropic unitary two-by-two matrix to the true anisotropy. If we define $\mathbf{J}^{-1} = \mathbf{J}_m^{-1} \mathbf{J}_t = \mathbf{P}_m \mathbf{\Lambda}_m^{-\frac{1}{2}} \mathbf{P}_m^T \mathbf{P}_t \mathbf{\Lambda}_t^{\frac{1}{2}} \mathbf{P}_t^T$ we can use a similar linear system as before, because we have $\mathbf{M}_t = \mathbf{J}_t^T \{\mathbf{J}_m^{-1}\}^T \; \mathbf{M}_m \; \mathbf{J}_m^{-1} \mathbf{J}_t$. For an isotropic true medium $\mathbf{J}_t^{-1}$ reduces to $\mathbf{I} c_h^{-1}$, where $\mathbf{I}$ is a two-by-two identity matrix, this agrees with eq. (27). Ideally, one would iteratively update the stencil corrections using the retrieved anisotropic velocities at each iteration. However, due to the effect of the unknown precise noise levels (Chartrand, 2011), such a scheme does not easily converge. Alternatively one could apply a first order correction for the underestimation as follows: use the derived underestimated anisotropic velocity map to compute a syntethic dataset, and use gradiometry to derive a new anisotropic velocity map that repeats the underestimation. Employ the relationship in eq. (36) to derive a transform that predicts the underestimation. Lastly, apply the inverse of this transform to the original retrieved map.

We illustrate this procedure in Fig. 6b-6d. Fig. 6c contains the secondary derived anisotropic velocity map underestimating the correct values from Fig. 6b. The recovered positive anoma-

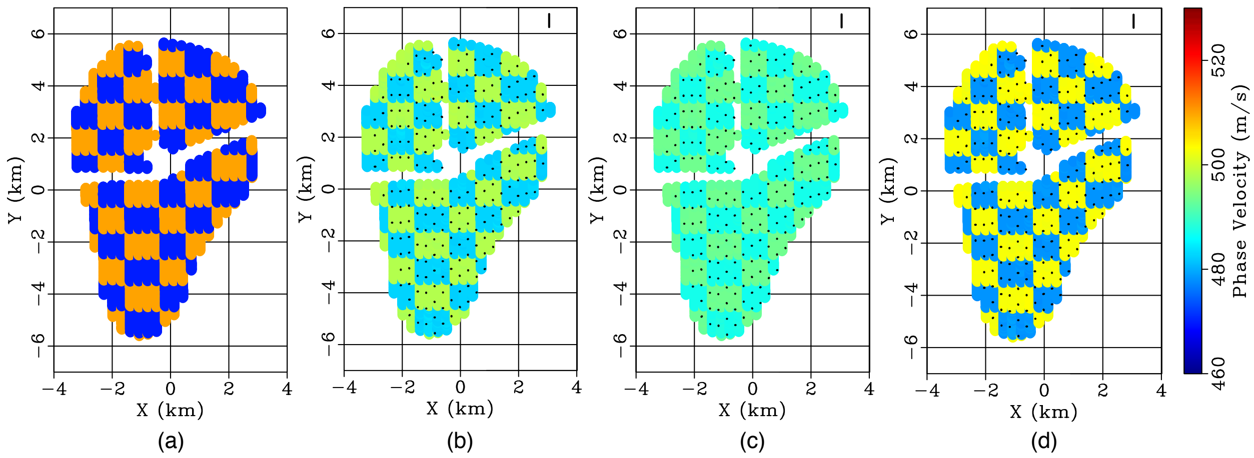

Figure 6. Checkerboard test for anomaly magnitude. Colour indicates isotropic component of velocity; dashes indicate magnitude and fast-direction of anisotropy (dash in upper right corner indicates 10% magnitude). a) Input isotropic velocity, with 5% anomaly magnitude. b) Anisotropic velocity map obtained using a synthetic created using the medium parameters of the isotropic velocity map in (a) and calibrated finite difference stencils, underestimating the anomalies (positive anomalies are recovered as 2.6% and negative anomalies are recovered as 2.4%). c) Anisotropic velocity map obtained using a synthetic created using the medium parameters of the anisotropic velocity map in (b), underestimating the anomalies again (positive anomalies are recovered as 1.6% and negative anomalies are recovered as 1.5%). d) Final anisotropic velocity map using the calibrated finite difference stencils plus anomaly-magnitude correction (positive anomalies are recovered as 3.2% and negative anomalies are recovered as 3.0%).

lies have a 1.6% magnitude, while the recovered negative anomalies have a 1.5% magnitude. The derived transform predicts Fig. 6c from Fig. 6b. By assuming that the degree of underestimation of anisotropy is consistent at models with larger anisotropy than the model we obtained in Fig. 6b, we apply the inverse of this transform to Fig. 6b resulting in Fig. 6d. The retrieved positive positive anomalies have a 3.2% magnitude, while the recovered negative anomalies have a 3.0% magnitude (still short of the original 5% anomaly magnitude).

Though the retrieved anomaly magnitudes remain underestimated, they are closer to the true anomaly magnitudes. This procedure relies on linearity of the underestimation with anomaly magnitude. But because the stencil error is non-linear with wavelength, the underestimation increases for larger anomaly magnitudes (see Fig. S1) in the supplemental material which shows the underestimation as a function of anomaly magnitude).

4 FIELD DATA EXAMPLE AT EKOFISK FIELD

Ekofisk field is one of the largest hydrocarbon fields in the North Sea, it was Norway's first producing field in 1971 (Van den Bark & Thomas, 1979) and has a projected lifespan exceeding year 2050. Rapid pressure depletion in the early phase of production and weakening due to subsequent water injection caused more than 9 m of seafloor subsidence over the Ekofisk field (Herwanger & Horne, 2009; Lyngnes et al., 2013). The subsidence is known to dominate the pattern in the anisotropic Scholte wave phase velocities in the near-surface (Kazinnik et al., 2014; De Ridder et al., 2015).

An OBC array was installed at Ekofisk in 2010 for the purposes of repeated seismic surveying (Eriksrud, 2010). The cables are buried in mud on the seafloor and the stations generally exhibit similar coupling to the sea floor. The characteristics of the microseism energy recorded by this array are well known (De Ridder & Biondi, 2015a; De Ridder et al., 2015). It was found that the pressure sensors record strong microseisms at frequencies between 0.35 and 1.35 Hz. This energy is dominated by fundamental-mode Scholte waves propagating along the seafloor. Below 0.8 Hz these waves are recorded unaliased in both the in-line and cross-line directions. No strong sources of seismic energy were found within the array in the microseism frequency range 0.35 to 1.35 Hz.

A recording of 10 minutes by the pressure sensors of the Ekofisk array was bandpass filtered between 0.6 Hz and 0.8 Hz using a Hann taper in the frequency domain, the data are downsampled to a 10 Hz sampling rate keeping the error in the temporal finite difference stencil small. Ten minutes were found to be sufficient to yield a map of isotropic phase velocities using wavefield gradiometry (De Ridder & Biondi, 2015b). We investigate the nature of the directionality of the ambient seismic field for a short recording of ten minutes by a beamform experiment consisting of plane wave stacks for planes defined by a moveout, azimuth and intercept time, i.e., a Tau-P transformation. Finally, we sum the absolute value of the plane wave stacks over all intercept times to form an image as a function of moveout and azimuth which is defined by horizontal slowness in both spatial directions (Fig. 7) (Kostov & Biondi, 1987; Rost & Thomas, 2002). Averaged over as little as 10 minutes, there

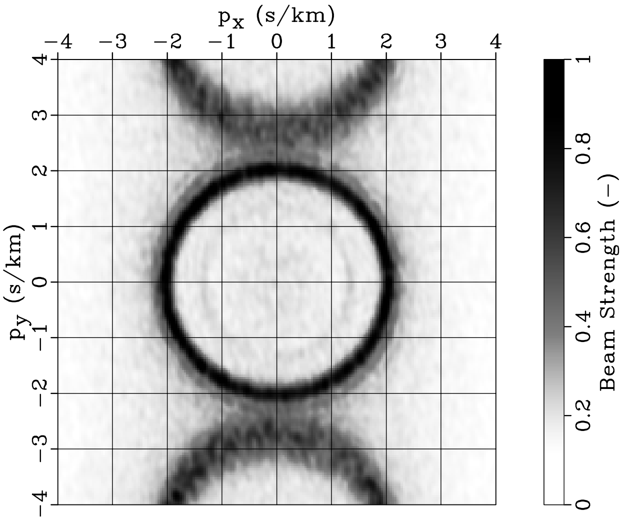

Figure 7. Beam steering image obtained by plane-wave stacking with different moveout velocities and directions, using 10 minutes of data and all stations of the array.

is no obvious preferential direction in the ambient seismic noise: the waves are incident on the array from all directions approximately equally strongly. The two circles above and below the center circle are aliasing ghost images of the same surface wave energy. The faint inner ring visible in Fig. 7 is the manifestation of energy of a higher surface wave mode (traveling with approximately 770 m/s), this energy is neglected in this study.

First, we solved the linear inverse system (eq. 2) for isotropic velocities with eqs. (5) to (7), without calibrated finite difference stencils. Second, we solved the linear system (eq. 2) with eqs. (17) to (19) for an anisotropic velocity map (Fig. 8a), using the solution of the isotropic case as the background velocity map. We find velocities that are much higher than the known average velocity from dispersion analysis. Furthermore, we find an anisotropic pattern where the fast-directions are generally oriented perpendicular to the cables. This is expected from the synthetic plane wave example above (compare to Fig. 2a). We then use the calibrated stencils, first solving the linear system (eq. 2) with eqs. (5) to (6) using eq. (29), then solving the linear system (eq. 2) with eqs. (30) to (35), and we obtain the anisotropic velocity map in Fig. 8b. Finally, we model synthetic plane waves satisfying the recovered anisotropic medium parameters in Fig. 8b, and follow the anisotropic gradiometry procedure to recover a map with underestimated anisotropic and anomaly magnitudes. We compute the transform

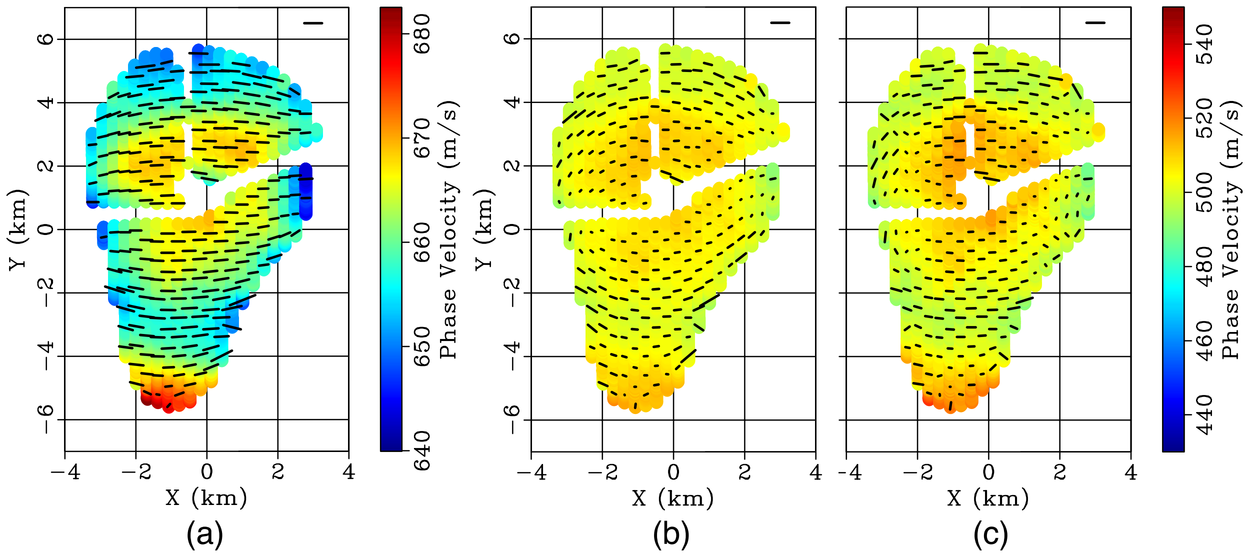

Figure 8. Field data result on Ekofisk's OBC array. Colour indicates isotropic component of velocity; dashes indicate magnitude and fast-direction of anisotropy (dash in upper right corner indicates 10% magnitude). a) Velocity map recovered with finite difference stencils without calibration. b) Velocity map recovered using the calibrated finite difference stencils. c) Final velocity map recovered using the calibrated finite difference stencils plus anomaly-magnitude correction.

estimating the underestimation and apply the inverse to the medium parameters in Fig. 8b to yield Fig. 8c. The magnitude of the velocity anomaly in the center of the array, and the magnitude of anisotropy oriented in-line at the left and right flanks of the array increased notably from Fig. 8b.

5 DISCUSSION

In principle, directionality in the ambient seismic noise will bias the inverted seismic velocities because the stencil error is directionally dependent. In this manuscript, we have given the plane waves from all directions equal weight when computing the synthetic example in Fig. 2. However, an estimate for the directional distribution can in principle be used as weights in the implicit regression to compute the bias of the array geometry, and thus be taken into account when computing the calibration for the finite difference stencils. The beamform experiment on the Ekofisk data provided the basis for not introducing such a weighting scheme in the field data application as the noise appeared to be equally distributed with azimuth. Ideally, the stencil calibration is iterated using the recovered anisotropic velocities to end with a set of finite difference stencils optimized for the recovered velocities. However, we found that this scheme does not generally converge. We conclude that this was probably due to the presence of noise in the field data because we observed that zero mean Gaussian distributed noise in the data causes a velocity bias (Fig. 5). This is a result of the error in finite difference stencils not being a linear function of the underlying wavelength (Fig. 3).

Generally, the computational costs of seismic noise gradiometry are relatively low compared to other techniques to image using ambient seismic noise. Seismic noise gradiometry requires only short recordings (De Ridder & Biondi, 2015b), and the regression operation itself is also kept computationally efficient by posing the finite differences on the irregular station geometry itself, by-passing the need for an interpolation scheme. Another argument for avoiding spatial interpolation is the inherent imposition of a usually non-physical model for seismic wavefields when electing an interpolation scheme. It would be physically most accurate to base an interpolation scheme on the wave equation itself, however that requires a priori knowledge of the underlying wave velocities. The total computational costs in our implementation are dominated by the inversion for anisotropic velocities because the anisotropic model space is three times larger then the isotropic model space, and the matrix in eq. (20) is nine times larger then the matrix in eq. (8). We used an LU decomposition to solve the matrix inversion, but employing Krylov subspace techniques may be a faster alternative.

Measurements of near-surface anisotropy are typically of interest for near-surface hazard monitoring (Barkved, 2012) and to infer geomechanical changes in the reservoir and overburden (Herwanger & Horne, 2009). These results match qualitatively with those found by an eikonal tomography on travel-time surfaces extracted from noise correlations (De Ridder & Biondi, 2015a), and critically refracted P waves, PS converted waves, surface wave analysis of controlled source seismic (Van Dok, 2003; Kazinnik et al., 2014). The circular pattern in azimuthal anisotropy has also been observed in seismic noise correlation tomography studies at nearby Valhall field (Mordret et al., 2013b; De Ridder 2014).

The resolution of wavefield gradiometry is limited by the stencil span from the assumption of homogeneity over the stencil span: in this study based on the Ekofisk OBC array this is at 800 m. In practice, the scattered wavefield due to subsurface changes is neglected, and we recover a spatially averaged anisotropic phase velocity map revealing spatially varying properties up to the resolution of the stencil span.

We solved for a phase velocity map at 0.7 Hz, but the procedure could be repeated for different frequencies mapping dispersion curves throughout the array. These surface wave dispersion curves could be inverted for depth structure (Kennett, 1976). However, in practice this may be difficult due to aliasing at higher frequencies, and spurious geophone sensitivity far below the natural frequency of each sensor.

Because there is no technique to measure particle velocity throughout the subsurface of the earth, seismic gradiometry based on the three dimensional elastodynamic wave equation, eq. (1), with the aim of imaging elastic properties throughout the medium remains illusive (Curtis & Robertsson, 2002; Muijs et al., 2003). However, in medical sciences a similar technique named elastography is used to extract the local stiffness from measurements of strains due to an induced stress, which has found wide application for the purposes of for example examining prostrate lesions, arteries, and tumors (Garra et al., 1997; De Korte et al., 1998; Pesavento & Lorenz, 2001; DeWall, 2013). Specifically, magnetic resonance elastography is based on tracking waves through human tissue for finding elastic parameters (Manduca et al., 2001).

6 CONCLUSIONS

Dense seismic networks deployed on the surface of the earth allow surface waves to be measured unaliased in time and space. These recordings permit estimation of the spatial derivative of surface-wave wavefields by finite differences, thus providing the ingredients needed to invert an elliptically anisotropic, two-dimensional wave equation for local medium properties. An advantage of this method is that it permits short recordings of surface-wave noise to be inverted. The main challenge is the error caused by the spatial FD stencils: this causes an overall anisotropic velocity error, and leads to the under-estimation of isotropic velocities. We formulated a two step approach to calibrate finite difference stencils, and perform a first order correction for the velocity anomaly magnitudes. The method is a promising technique for studying changes in the subsurface geomechanical strain resulting from time dependent phenomena operating at short time-scales, which in the example herein are likely to be due to subsidence-related extension.

ACKNOWLEDGMENTS

The authors thank Giovanni Meles from the School of GeoSciences at the University of Edinburgh, the members of the Applied and Computational Mathematics group at the University of Edinburgh, and Olaf Knoth and Ali Tura from ConocoPhillips for helpful discussions and suggestions. The authors thanks the sponsors of the Edinburgh Interferometry Project for support and access to the field data. The authors thank ConocoPhillips Skandinavia AS and the PL018 Partnership (Total E&P Norge AS, ENI Norge AS, Statoil Petroleum AS, and Petoro AS) for permission to show Ekofisk field data. SdR thanks the School of Mathematics of the University of Edinburgh for financial support through a Whittaker Fellowship. The authors are grateful to Cedric Schmelzbach, an anonymous reviewer, and the editor for helpful suggestions and constructive comments that improved this manuscript.

REFERENCES

Aki, K., 1957. Space and time spectra of stationary stochastic waves, with special reference to microtremors, *Bulletin of the Earthquake Research Institute*, **35**, pp. 415–456.

Anderson, D. L., 1961. Elastic wave propagation in layered anisotropic media, *Journal Geophysical Research*, **66**, pp. 2953–2963.

Ando, M., Ishikawa, Y., Wada, H., 1980. S-wave anisotropy in the upper mantle under a volcanic area in Japan, *Nature*, **286**, pp. 43–46.

Barkved, O. I., 2012. Seismic surveillance for reservoir delivery from a practitioners point of view, *EAGE Publications bv*, 273 pages.

Boness, N. L. & Zoback, M. D., 2004. Stress-induced seismic velocity anisotropy and physical properties in the safod pilot hole in parkfield, ca, *Geophysical Research Letters*, **31**(15), L15S17, 4 pages.

Brenguier, F., Campillo, M., Hadziioannou, C., Shapiro, N. M., Nadeau, R. M., & Larose, E., 2008. Postseismic relaxation along the san andreas fault at parkfield from continuous seismological observations, *Science*, **321**(5895), pp. 1478–1481.

Brenguier, F., Campillo, M., Takeda, T., Aoki, Y., Shapiro, N. M., Briand, X., Emoto, K., & Miyake, H., 2014. Mapping pressurized volcanic fluids from induced crustal seismic velocity drops, *Science*, **345**(6192), pp. 80–82.

Chartrand, R., 2011. Numerical Differentiation of Noisy, Nonsmooth Data, *ISRN Applied Mathematics/*, vol. **2011**, Article ID 164564, 11 pages.

Christensen, N. I. & Lundquist, S. M., 1982. Pyroxene orientation within the upper mantle , *Geological Society of America Bulletin*, **93**(4), pp. 279-288.

Crampin, S., Evans, R., Üçer, B., Doyle, M., Davis, J. P., Yegorkinaparallel, G. V., & Miller, A., 1980b. Observations of dilatancy-induced polarization anomalies and earthquake prediction, *Nature*, **286**, pp. 874–877.

Crampin, S., McGonigle, R., Bamford, D., 1980a. Estimating crack parameters from observations of P-wave velocity anisotropy, *Geophysics*, **45**(3), pp. 345–360.

Curtis, A. & Robertsson, J. O. A., 2002. Volumetric wavefield recording and wave equation inversion for near-surface material properties, *Geophysics*, **67**(5), pp. 1602–1611.

de Korte, C., van der Steen, A. F. M., Céspedes, E. I., & Pasterkamp, G., 1998. Intravascular ultrasound elastography in human arteries: experience in vitro, *Ultrasound in Medical and Biololgy*, **24**, pp. 401–408.

de Ridder, S. A. L., 2014. *Passive seismic surface-wave interferometry for reservoir-scale imaging*, Ph.D. thesis, Stanford University, 199 pages.

de Ridder, S. and J. Dellinger, 2011. Ambient seismic noise eikonal tomography for near-surface imaging at valhall, *The Leading Edge*, **30**(5), pp. 506–512.

de Ridder, S. A. L. & Biondi, B. L., 2015a. Ambient seismic noise tomography at ekofisk, *Geophysics*, **80**(6), pp. B167–B176.

de Ridder, S. A. L. & Biondi, B. L., 2015b. Near-surface scholte wave velocities at ekofisk from short noise recordings by seismic noise gradiometry, *Geophysical Research Letters*, **42**(17), pp. 7031–7038.

de Ridder, S. A. L., Biondi, B. L., & Nichols, D., 2015. Elliptical-anisotropic eikonal phase velocity tomography, *Geophysical Research Letters*, **42**(3), pp. 758–764.

Dellinger, J. A., 1991. *Anisotropic Seismic Wave Propagation*, Ph.D. thesis, Stanford University, 184 pages.

DeWall, R. J., 2013. Ultrasound Elastography: Principles, Techniques, and Clinical Applications, *Critical Reviews in Biomedical Engineering*, **41**(1), pp. 1–19.

Edme, P. & Yuan, S., 2016. Local dispersion curve estimation from seismic ambient noise using spatial gradients, *Interpretation*, **4**(3), pp. SJ17-SJ27.

Eriksrud, M., 2010. Towards the optical seismic era in reservoir monitoring, *First Break*, **28**, pp. 105–111.

Forsyth, D. W. & Li, A., 2013. Array Analysis of Two-Dimensional Variations in Surface Wave Phase Velocity and Azimuthal Anisotropy in the Presence of Multipathing Interference, in *Seismic Earth: Array Analysis of Broadband Seismograms*, pp. 81–97, American Geophysical Union.

Galetti, E., Curtis, A., Meles, G. A., & Baptie, B., 2015. Uncertainty loops in travel-time tomography from nonlinear wave physics, *Physical Review Letters*, **114**, 148501.

Garra, B. S., Céspedes, E. I., Ophir, J., Spratt, S. R., Zuurbier, R. A., Magnant, C. M., & Pennanen, M. F., 1997. Elastography of breast lesions: Initial clinical results, *Radiology*, **202**, pp. 79–86.

Gouédard, P., Yao, H., Ernst, F., & van der Hilst, R. D., 2012. Surface wave eikonal tomography in heterogeneous media using exploration data, *Geophysical Journal International*, **191**(2), pp. 781–788.

Hansen, P. & OLeary, D., 1993. The use of the L-Curve in the regularization of discrete ill-posed problems, *SIAM J. Sci. Comput.*, **14**, pp. 1487–1503.

Helbig, K., 1983. Elliptical anisotropy-its significance and meaning, *Geophysics*, **48**(7), pp. 825–832.

Herwanger, J. V. & Horne, S. A., 2009. Linking reservoir geomechanics and time-lapse seismics: Predicting anisotropic velocity changes and seismic attributes, *Geophysics*, **74**(4), pp. W13–W33.

Hobiger, M., Wegler, U., Shiomi, K., & Nakahara, H., 2016. Coseismic and post-seismic velocity changes detected by passive image interferometry: comparison of one great and five strong earthquakes in japan, *Geophysical Journal International*, **205**(2), pp. 1053–1073.

Huiskamp, G., 1991. Difference formulas for the surface Laplacian on a triangulated surface, *Journal of Computational Physics*, **95**, pp. 477–496.

Kazinnik, R., Roy, B., Tura, A., Vedvik, L., & Knoth, O., 2014. Near surface velocities at Ekofisk from Scholte and refracted wave analysis, in *SEG, Technical Program Expanded Abstracts*, pp. 2036–2039.

Kennett, B. L. N., 1976. The inversion of surface wave data, *pure and applied geophysics*, **114**(5), pp. 747–751.

Korneev, V. & Glubokovskikh, S., 2013. Seismic velocity changes caused by an overburden stress, *Geophysics*, **78**(5), pp. WC25–WC31.

Kostov, C. & Biondi, B., 1987. *Improved resolution of slant stacks using beam stacks*, chap. 247, pp. 792–794, Society of Exploration Geophysicists.

Langston, C. A., 2007a. Spatial gradient analysis for linear seismic arrays, *Bulletin of the Seismological Society of America*, **97**(1B), pp. 265–280.

Langston, C. A., 2007b. Wave gradiometry in two dimensions, *Bulletin of the Seismological Society of America*, **97**(2), pp. 401–416.

Langston, C. A., 2007c. Wave gradiometry in the time domain, *Bulletin of the Seismological Society of America*, **97**(3), pp. 926–933.

Lawson, C.L., Hanson, R.J., 1974 Solving Least Squares Problems, Prentice Hall, Englewood Cliffs, NJ.

Lin, F.-C. & Ritzwoller, M. H., 2011. Helmholtz surface wave tomography for isotropic and azimuthally anisotropic structure, *Geophysical Journal International*, **186**(3), pp. 1104–1120.

Lin, F.-C., Ritzwoller, M. H., & Snieder, R., 2009. Eikonal tomography: surface wave tomography by phase front tracking across a regional broad-band seismic array, *Geophysical Journal International*, **177**, pp. 1091–1110.

Liu, Y. & Holt, W. E., 2015. Wave gradiometry and its link with helmholtz equation solutions applied to USarray in the eastern U.S., *Journal of Geophysical Research: Solid Earth*, **120**(8), pp. 5717–5746.

Lyngnes, B., Landa, H., Ringen, K., & Haller, N., 2013. Life of Field Seismic at Ekofisk - Utilizing 4D seismic for evaluating well target, in *75^{th} Conference and Exhibition, EAGE, Extended Abstracts*, We 12 09.

Manduca, A., Oliphant, T., Dresner, M., Mahowald, J., Kruse, S., Amromin, E., Felmlee, J., Greenleaf, J., & Ehman, R., 2001. Magnetic resonance elastography: Non-invasive mapping of tissue elasticity, *Medical Image Analysis*, **5**, pp. 237–254.

Montagner, J.-P., Jobert, N., 1988. Vectorial tomographyII. Application to the Indian Ocean, *Geophysical Journal International*, **94**(2), pp. 309–344.

Montagner, J.-P., Nataf, H.-C., 1986. A simple method for inverting the azimuthal anisotropy of surface waves, *Journal of Geophysical Research: Solid Earth*, **91**(B1), pp. 511–520.

Montagner, J.-P., Nataf, H.-C., 1988. Vectorial tomographyI. Theory, *Geophysical Journal International*, **94**(2), pp. 295–307.

Montagner, J.-P., Tanimoto, T., 1990. Global anisotropy in the upper mantle inferred from the regionalization of phase velocities, *Journal of Geophysical Research: Solid Earth*, **95**(B4), pp.

4797–4819.

Mordret, A., Shapiro, N., Singh, S., Roux, P., & Barkved, O. I., 2013a. Helmholtz Tomography of ambient noise surface wave data to estimate Scholte wave phase velocity at Valhall Life of the Field, *Geophysics*, **78**(2), pp. WA99–WA109.

Mordret, A., N. Shapiro, S. Singh, P. Roux, J.-P. Montagner, & O. I. Barkved, 2013b. Azimuthal anisotropy at Valhall: The Helmholtz equation approach, *Geophysical Research Letters*, **40**(3), pp. 2636-2641.

Muijs, R., Robertsson, J. O. A., Curtis, A., & Holliger, K., 2003. Near-surface seismic properties for elastic wavefield decomposition: Estimates based on multicomponent land and seabed recordings, *Geophysics*, **68**(6), pp. 2073–2081.

Pesavento, A. & Lorenz, A., 2001. Real time strain imaging - a new ultrasonic method for cancer detection: first study results, in *IEEE Ultrasonic Symposium Proceedings*, pp. 1647–1652.

Peselnick, L. & Nicolas, A., 1978. Seismic anisotropy in an ophiolite peridotite: Application to oceanic upper mantle, *Journal of Geophysical Research: Solid Earth*, **83**(B3), pp. 12271235.

Plessix, R., Cao, Q., 2011. A parametrization study for surface seismic full waveform inversion in an acoustic vertical transversely isotropic medium, *Geophysical Journal International*, **185**(1), pp. 539–556.

Poppeliers, C., Punoševac, P., & Bell, T., 2013. Three-dimensional seismic-wave gradiometry for scalar waves, *Bulletin of the Seismological Society of America*, **103**(4), pp. 2151–2160.

Rost, S. & Thomas, C., 2002. Array seismology: Methods and applications, *Reviews of Geophysics*, **40**(3), p. 2–1–2–27.

Sieminski, A., Liu, Q., Trampert, J., Tromp, J., 2007. Finite-frequency sensitivity of surface waves to anisotropy based upon adjoint methods, *Geophysical Journal International*, **168**(3), pp. 1153–1174.

Smith, M. L. & Dahlen, F. A., 1973. The azimuthal dependence of Love and Rayleigh wave propagation in a slightly anisotropic medium, *Journal of Geophysical Research*, **78**(17), pp. 3321–3333.

Sollberger, D., Schmelzbach, C., Robertsson, J. O. A., Greenhalgh, S. A, Nakamura, Y., Khan, A., 2016. The shallow elastic structure of the lunar crust: New insights from seismic wavefield gradient analysis, *Geophysical Research Letters*, **43**(19), pp. 10,078–10,087.

Tanimoto T., Anderson, D. L., 1984. Mapping convection in the Mantle, *Geophysical Research Lettyers*, **11**(4), pp. 287–290.

Teanby, N., Kendall, J.-M., Jones, R. H., & Barkved, O., 2004. Stress-induced temporal variations in seismic anisotropy observed in microseismic data, *Geophysical Journal International*, **156**(3), pp. 459–466.

Tsvankin, I. D., 2011. 1. normal-moveout (nmo) ellipse and generalized dix equation, in *Seismology of Azimuthally Anisotropic Media and Seismic Fracture Characterization*, chap. 1, pp. 1–43, eds Tsvankin, I. & Grechka, V., Society of Exploration Geophysicists.

van den Bark, E. & Thomas, O. D., 1979. Ekofisk: First of the giant oilfields in western europe, in *Giant Oil and Gas Fields of the Decade*, pp. 195–224, ed. Halbouty, M. T., American Association of Petroleum Geologists.

Van Dok, R., Gaiser, J., & Byerley, G., 2003. Near-surface shear-wave birefringence in the North Sea: Ekofisk 2D/4C test, *The Leading Edge*, **22**, pp. 1236–1242.

Vinnik, L. P., Farra, V., & Romanowicz, B. , 1989. Azimuthal anisotropy in the earth from observations of SKS at GEOSCOPE and NARS broadband stations, *Bulletin of the Seismological Society of America*, **191**(2), pp. 1542–1558.

Wielandt, E., 1993. Propagation and structural interpretation of non-plane waves, *Geophysical Journal International*, **113**(1), pp. 45–53.

Wüstefeld, A., Bokelmann, G., Barruol, G., Montagner, J.-P., 2009. Identifying global seismic anisotropy patterns by correlating shear-wave splitting and surface-wave data, *Physics of the Earth and Planetary Interiors*, **176**, pp. 198–212.

submitted to *Geophys. J. Int.*

Seismic Gradiometry using Ambient Seismic Noise in an Anisotropic Earth: Supplementary material

S.A.L. de Ridder[1] and A. Curtis[2]

[1] *School of Mathematics and Maxwell Institute for Mathematical Sciences,University of Edinburgh, Edinburgh EH9 3FD, United Kingdom.*

[2] *School of GeoSciences and Grant Institute of Earth Science, University of Edinburgh, Edinburgh EH9 3FE, United Kingdom.*

Received 2017 February 17; in original form 2016 September 7

We conducted a series of synthetic experiments to map the underestimation of isotropic and anisotropic velocity anomalies. First, we created a series of synthetic datasets with a checkerboard pattern as for the example in Fig.5. We measure the magnitude of the recovered positive and negative anomalies versus the magnitude used to create the synthetic dataset. We systematically underestimate the positive and negative anomalies, and the underestimation is not a linear function of anomaly magnitude as it increases with larger input anomaly magnitude (coarse and fine dashes in Fig. S1). Second, we created a series of synthetic datasets with anisotropy as in the example in Fig.4. We measured the recovered anisotropy magnitude, versus the anisotropy magnitude used to create the synthetic dataset. We systematically underestimate the anisotropy magnitude, and the underestimation is not a linear function of anisotropy magnitude (solid curve in Fig. S1).

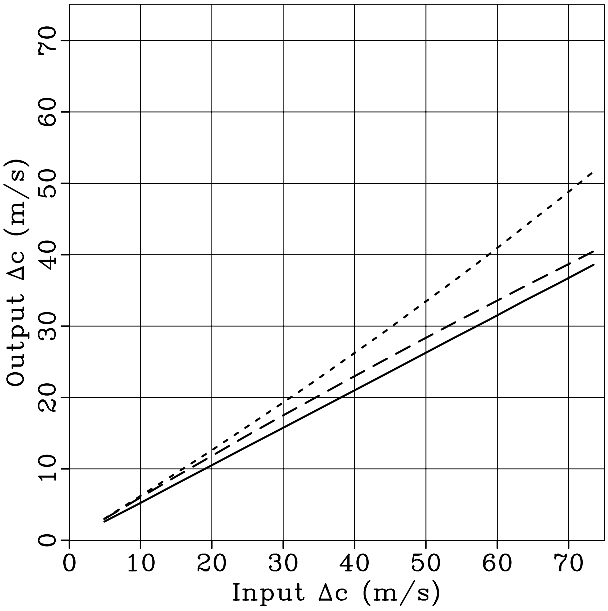

Figure S1. Recovered minimum (coarse dashes) and maximum (fine dashes) anomaly in magnitudes versus input anomaly magnitude determined by repeated checkerboard tests recovering isotropic velocities. Recovered anisotropy magnitude (solid curve) defined as the difference between the maximum and minimum wave speeds, versus input anisotropy magnitudes in repeated tests recovering anisotropic velocities.